



Catalytic performance and characterization of Co–Fe bcc alloy nanoparticles prepared from hydrotalcite-like precursors in the steam gasification of biomass-derived tar

Lei Wang^{a,b}, Jinhai Chen^a, Hideo Watanabe^c, Ya Xu^d, Masazumi Tamura^a, Yoshinao Nakagawa^a, Keiichi Tomishige^{a,*}

^a Department of Applied Chemistry, School of Engineering, Tohoku University, 6-6-07, Aoba, Aramaki, Aoba-ku, Sendai 980-8579, Japan

^b Shaanxi Coal and Chemical Technology Institute Co., Ltd., No. 2 Jinye 1st Road, High-Tech District, Xi'an 710070, China

^c Graduate School of Pure and Applied Sciences, University of Tsukuba, 1-1-1, Tennodai, Tsukuba 305-8573, Ibaraki, Japan

^d National Institute of Materials Science, 1-2-1, Sengen, Tsukuba 305-0047, Ibaraki, Japan

ARTICLE INFO

Article history:

Received 6 February 2014

Received in revised form 14 June 2014

Accepted 16 June 2014

Available online 23 June 2014

Keywords:

Co–Fe alloy

Hydrotalcite

Steam gasification

Biomass

Tar

ABSTRACT

The Co–Fe/Mg/Al catalysts were prepared from the hydrotalcite-like compounds containing Co, Fe, Mg and Al, and applied to the steam gasification of biomass-derived tar. The characterization using TPR, TPO, XRD, H₂ adsorption, TEM and EXAFS indicates that the Co–Fe/Mg/Al catalysts have a nanocomposite structure of the Co–Fe bcc alloy particles and the oxide particles of MgAl₂O₄-based solid solution after the reduction, where Co metal atoms can substitute partially Fe metal sites in bcc Fe metal regarding the Co–Fe bcc alloy particles. The composition of the Co–Fe/Mg/Al catalysts was optimized on the basis of the activity tests. The optimized Co–Fe/Mg/Al catalyst exhibited higher catalytic performance than the reported catalysts such as Co–Fe/α-Al₂O₃, Co/Mg/Al, Ni–Fe/Mg/Al in terms of activity and resistance to coke deposition. This behavior can be explained by the formation of the Co–Fe bcc alloy nanoparticles with rather uniform composition on MgAl₂O₄-based solid solution.

© 2014 Elsevier B.V. All rights reserved.

1. Introduction

Gasification of biomass is an important step for the production of fuels and chemicals from biomass by utilizing C1 chemistry including Fischer–Tropsch synthesis, methanol synthesis and so on [1,2]. Reaction conditions for the gasification of biomass are strongly dependent on gasifying agents. In the case of the gasification of biomass with air, the reaction temperature can be high when exothermal or autothermal conditions are applied. One of the disadvantages in the gasification with air is the dilution of the product gas with N₂ in air, which can decrease the efficiency in the utilization of the product gas such as power generation, chemical conversion and so on. On the other hand, the steam gasification of biomass-derived tar is highly endothermic and needs the external heat supply from the outside of the reactor. From the viewpoint of the decrease in the input energy for the heat supply, lower reaction temperature is more favorable. One of the effective

methods for the decrease of the reaction temperature is the catalytic steam gasification, where the gasification reaction can be promoted by the presence of catalysts. In particular, it has been reported that metal-catalyzed steam gasification can decrease the reaction temperature remarkably [3,4]. Various efforts have been made for the development of the Ni-based catalysts for the steam gasification of biomass-derived tar, for example, nano-NiO/γ-Al₂O₃ and nano-Ni–La–Fe/Al₂O₃ [5], NiO–MgO solid solution catalyst [6], and NiO-loaded calcined dolomite catalysts [7], Ni catalysts modified with CeO₂ [8–12], MnO_x [13], Fe [14,15]. At the same time, Co catalysts for the steam gasification of biomass-derived tar also have been developed, and the performance has been evaluated using real biomass [16–19] or its model compounds such as naphthalene [20,21], toluene [22,23], ethanol [24–26], methanol [27], acetic acid [28] and so on.

A possible method for the catalyst development is to utilize the alloy formation of the active metal species with another metal [29–32]. An example of the catalyst development is the modification of Ni with Fe [14,15,33–37]. The performance of the Ni catalysts modified with Fe is usually dependent on the additive amount of Fe, and the addition of the optimized amount of Fe enhances the performance remarkably. It has been reported that Ni–Fe alloys

* Corresponding author. Tel.: +81 22 795 7214; fax: +81 22 795 7214.

E-mail addresses: tomi@erec.che.tohoku.ac.jp, tomi@tulip.sannet.ne.jp (K. Tomishige).

are formed. In the case of the catalysts prepared by a conventional co-impregnation method, the composition of each Ni–Fe alloy particles is not uniform [14]. On the other hand, the composition of Ni–Fe alloy particles formed via hydrotalcite-like precursors is rather uniform, and Ni–Fe fcc alloy was only formed by the reduction pretreatment in wide composition range ($0 < \text{Fe/Ni} \leq 1.5$) [15,37]. Regarding Co catalysts, it has been recently reported that the modification of Co with Fe promoted the gasification and its related reactions [19,23,25,38]. Like the case of Ni–Fe catalysts, the composition of Co–Fe alloy particles is not uniform on the catalysts prepared by the conventional co-impregnation method [19]. It should be noted that both Co–Fe fcc and bcc alloy phases were formed simultaneously, and the composition of Co–Fe fcc and bcc alloys were determined to be Co rich and Fe rich, respectively. The ununiformity in the composition can be connected to the formation of the simultaneous formation of the two different phases. On the other hand, it has been recently reported that Co–Fe bcc alloy is contributable to high activity, although Co–Fe bcc alloy was oxidized more easily than Co–Fe fcc alloy because of the high molar ratio of Fe with higher oxygen affinity [23,39]. The purpose of the work is to prepare the Co–Fe catalysts having the Co–Fe bcc alloy phase by using hydrotalcite-like precursors, and then the catalysts were characterized and evaluated in the steam gasification of biomass-derived tar.

2. Experimental

2.1. Catalyst preparation

Hydrotalcite-like compounds containing Co and Fe were prepared by coprecipitation of the nitrates of metal components on the basis of the previous reports [40,41] with minor modifications. The mixed aqueous solution of $\text{Mg}(\text{NO}_3)_2 \cdot 6\text{H}_2\text{O}$ (Wako), $\text{Al}(\text{NO}_3)_3 \cdot 9\text{H}_2\text{O}$ (Wako), $\text{Fe}(\text{NO}_3)_3 \cdot 9\text{H}_2\text{O}$ (Wako) and $\text{Co}(\text{NO}_3)_2 \cdot 6\text{H}_2\text{O}$ (Wako) was slowly added in drops into a beaker containing Na_2CO_3 aq under stirring at room temperature and a constant pH of 10 ± 0.5 , where the pH of the solution was adjusted with NaOH aq (2 M). The resulting suspension was then kept at room temperature for 24 h. The resulting precipitate was filtered and washed several times with de-ionized water and dried at 383 K for one night. The precipitate was ground to fine powders and then calcined at 1073 K for 5 h in a static air atmosphere. The powders were pressed to a disk, crushed and then sieved to particles with 30–60 mesh size (0.3–0.6 mm). This is represented as Co–Fe/Mg/Al. The Co content in Co–Fe/Mg/Al is 12 wt% as a weight percentage, and the molar ratio of $(\text{Co} + \text{Mg})/(\text{Fe} + \text{Al})$ was fixed to be one on the basis of our previous report [41]. Here, the molar ratio of Fe/Co varied from 0.25 to 1.5. For comparison, Co/Mg/Al [41] and Ni–Fe/Mg/Al [37] samples were also prepared by co-precipitation of the nitrates of corresponding metal components, followed by drying and calcination at 1073 K for 5 h. The composition in terms of the atomic percentage of Co, Fe, Mg, Al of the catalysts is listed in Table 1. The catalysts are denoted using atomic percentage of each metal component like Co–Fe/Mg/Al (10–10/40/40). Here, the atomic percentage of the catalysts was assumed to be the same as that of the solution as prepared above. In our previous work, we determined the atomic percentage of hydrotalcite compounds prepared in a similar way and we verified that the atomic percentage of hydrotalcite compounds is almost the same as that of the corresponding solution [37]. The error margin of the molar ratio of Fe to Co can be estimated to be within 5%.

For the comparison, $\alpha\text{-Al}_2\text{O}_3$ supported Co–Fe catalyst was also prepared. The support material of $\alpha\text{-Al}_2\text{O}_3$ was prepared by the calcination of $\gamma\text{-Al}_2\text{O}_3$ (KHO-24, Sumitomo Chemical Co., Ltd, $133 \text{ m}^2/\text{g}$, grain size 2–3 mm) in air at 1423 K. After the calcination, it was crushed and sieved to particle sizes between 0.3 and 0.6 mm.

Table 1

Composition of Co–Fe/Mg/Al and Ni–Fe/Mg/Al catalysts.

Catalysts	Atomic percentage				(Co + Mg)/(Fe + Al) or (Ni + Mg)/(Fe + Al) atomic ratio
	Co or Ni	Fe	Mg	Al	
Co/Mg/Al (10/40/50)	10	0	40	50	1
Co–Fe/Mg/Al (10–2.5/40/47.5)	10	2.5	40	47.5	1
Co–Fe/Mg/Al (10–5/40/45)	10	5	40	45	1
Co–Fe/Mg/Al (10–7.5/40/42.5)	10	7.5	40	42.5	1
Co–Fe/Mg/Al (10–10/40/40)	10	10	40	40	1
Co–Fe/Mg/Al (10–12.5/40/37.5)	10	12.5	40	37.5	1
Co–Fe/Mg/Al (10–15/40/35)	10	15	40	35	1
Ni–Fe/Mg/Al (9.1–2.3/66/22.6)	9.1	2.3	66	22.6	3
Fe/Mg/Al (10/50/40)	0	10	50	40	1

The Co–Fe/ $\alpha\text{-Al}_2\text{O}_3$ catalyst was prepared by a co-impregnation method using a mixed aqueous solution of $\text{Co}(\text{NO}_3)_2 \cdot 6\text{H}_2\text{O}$ (Wako) and $\text{Fe}(\text{NO}_3)_3 \cdot 9\text{H}_2\text{O}$ (Wako). After the impregnation, the sample was dried at 383 K for 12 h followed by the calcination at 773 K for 3 h under air atmosphere. The loading amount of Co was 12 wt% Co and the loading amount of Fe was in the molar ratio of Fe/Co = 0.25 on the basis of the previous report [19], and the BET surface area was determined to be $10 \text{ m}^2/\text{g}$.

2.2. Activity test in the steam gasification of cedar wood

The elemental analysis of cedar wood was carried out by the Japan Institute of Energy. Cedar wood was ground with a ball mill to about 0.1–0.3 mm size. The moisture content of the cedar wood was 7.2% (JIS-K-2275). The dry-based composition by weight was C 50.8% (ASTM-D-5291), H 6.0% (ASTM-D-5291), N 0.2% (ASTM-D-5291), O 41.8% (ASTM D5622), and ash 1.1% (JIS-K-2272).

Catalytic performance was evaluated using a laboratory-scale continuous feeding dual-bed reactor that was described in our previous report [9,41], and the details of the procedure for catalytic performance evaluation in the steam gasification of biomass-derived tar have been also described [9,41]. The feeding condition of biomass particles were the same as that in our previous report [41]. The steam was also supplied to the reactor by the evaporation of water fed by a syringe pump ($555\text{--}1110 \mu\text{mol}/\text{min}$). The molar ratio of the feeding steam to feeding carbon in the biomass was denoted as S/C, and the conditions of S/C = 0.23–0.38 were applied. The molar ratio of the total steam (the feeding steam + the moisture in the biomass) to feeding carbon in the biomass was calculated to be 0.34–0.48.

The tests were performed under atmospheric pressure by using 0.3 g of catalyst. Co–Fe/Mg/Al (10–2.5/40/47.5–10–15/40/35), Co/Mg/Al (10/40/50) and Ni–Fe/Mg/Al (9.1–2.3/66/22.6) catalysts were reduced with H_2/N_2 (30/30 ml/min) mixed gas at 1073 K for 0.5 h before the activity test. The Co–Fe/ $\alpha\text{-Al}_2\text{O}_3$ catalyst was reduced at 773 K for 0.5 h using 30 ml/min H_2 before the activity test [19,22]. The test for the evaluation of the catalytic activity started with the biomass feeding and continued for 15 min. The formation rate of gaseous products was almost constant during 15 min on all the tested catalysts. The methods for the product gas collection and analysis were the same as those in our previous report [9]. After the activity test for 15 min, the amount of char accumulated in the primary bed and the amount of coke deposited on the catalyst surface were measured. The methods for the determination of char and coke amount were the same in our previous report [9]. The calculation method for tar yield was the same as that in our previous report [9]. In addition, the formation rate of $\text{CO} + \text{H}_2$ was also plotted in the results as a desired product in the steam

gasification. In order to evaluate the catalyst stability, the longer reaction time than 15 min and the regeneration of the deactivated catalysts were adopted. In particular, after the test for a specific time, the used catalysts were oxidized in O₂/N₂ (1/3) at 873 K for 60 min, and reduced subsequently at 1073 K or 773 K for 30 min, for the catalyst regeneration. The details are described in each result. After these regeneration procedures, the catalysts were used for the activity test again.

2.3. Catalyst characterization

Methods and procedures for temperature-programmed reduction (TPR) with H₂, and temperature-programmed oxidation (TPO) with O₂ were the same as those in our previous report [41]. The amount of O₂ consumption was used for the estimation of the reduction degree of Co and Fe species on the basis of the oxidation stoichiometry: $3\text{Co}^0 + 2\text{O}_2 \rightarrow \text{Co}_3\text{O}_4$ and $3\text{Fe}^0 + 2\text{O}_2 \rightarrow \text{Fe}_3\text{O}_4$ [42].

Methods and procedures for H₂ chemisorption experiments and XRD measurements were the same as those in our previous report [41]. For XRD measurements, the step-size was 0.01°, and 0.635 s per step was used.

Scanning transmission electron microscope (STEM) images and energy dispersive X-ray (EDX) analysis were taken by means of the instrument (JEM-2010F, JEOL) operated at 200 kV. The sample powders after the reduction were dispersed in 2-propanol by supersonic wave and put on Cu grids for STEM observation under air. Average particle size was calculated by $\sum n_i d_i^3 / \sum n_i d_i^2$ (d_i : particle size, n_i : number of particle with d_i) [14,43]. The spot size of EDX analysis is ~1 nm.

The Co *K*-edge and Fe *K*-edge extended X-ray adsorption fine structure (EXAFS) was measured at the BL01B1 station at SPring-8 with the approval of the Japan Synchrotron Radiation Research Institute (JASRI; Proposal No. 2012A1089, 2013A1048). The storage ring was operated at 8 GeV. A Si(111) single crystal was used to obtain a monochromatic X-ray beam. Two ion chambers filled with 85% N₂ and 15% Ar diluted with N₂ were used as detectors of I_0 and I , respectively. Samples for the EXAFS measurement were

prepared by pressing the mixture of the catalyst powder reduced at 1073 K with $\alpha\text{-Al}_2\text{O}_3$ powder to the disk with 50 mg. The thickness of the sample disks for the Co and Fe *K*-edge measurements was adjusted to be 0.2–0.4 mm (7 mm diameter) to give 1.3 and 1.2 edge jump, respectively. For the reduced catalysts, the sample disk was reduced again with H₂ at 773 K in a glass tube, and then sealed with polymer film under N₂ atmosphere, thus avoiding sample exposure to air. EXAFS spectra were collected in a transmission mode at room temperature. For EXAFS analysis, the oscillation was first extracted from the EXAFS data by a spline smoothing method. The oscillation was normalized by the edge height around 50 eV. The Fourier transformation of the k^3 -weighted EXAFS oscillation from k space to r space was performed over the range of 30–120 nm^{−1} to obtain a radial distribution function. The inversely Fourier filtered data were analyzed by a usual curve fitting method. In the case of Co *K*-edge EXAFS of the Co–Fe/Mg/Al catalyst, the contribution of both Co–Co and Co–Fe bonds is expected. However, it is impossible to distinguish between Co and Fe as a backscattering atom because their atomic numbers are close to each other [44,45]. Here, we represented this contribution as Co–Co (or –Fe), whose phase shift and the amplitude functions are extracted from Co metal. The curve fitting analysis of the Co–O bond was done by using NiO as a model compound. In the case of Fe *K*-edge EXAFS analysis of Co–Fe/Mg/Al catalysts, the Fe–Fe and Fe–Co bonds are also represented as Fe–Co (–or Fe) bond for the same reason mentioned above, and the phase shift and amplitude functions were also extracted from Co foil. The curve fitting analysis of the Fe–O bonds was also done by using NiO as a model compound. The analysis of EXAFS data was performed using the “REX2000” program (Rigaku Co. Version: 2.3.3).

3. Results and discussion

3.1. Catalyst characterization of fresh catalysts

Fig. 1A shows the XRD patterns of the as-synthesized Co–Fe/Mg/Al precursors with various compositions, together

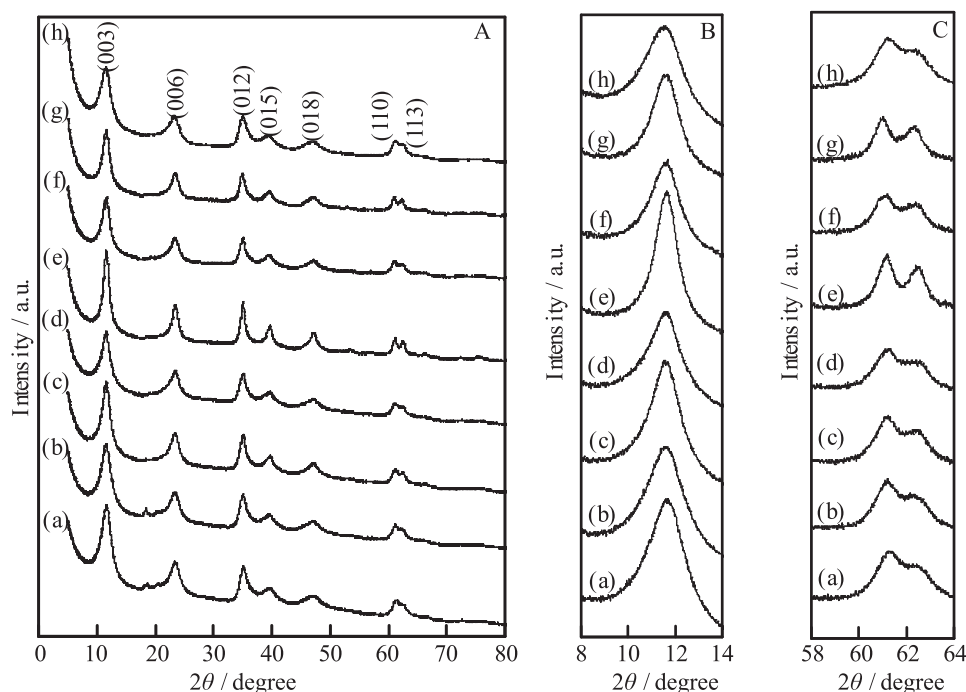


Fig. 1. (A) XRD patterns of the as-synthesized samples: (a) Co/Mg/Al(10/40/50), (b) Co–Fe/Mg/Al (10–2.5/40/47.5), (c) Co–Fe/Mg/Al (10–5/40/45), (d) Co–Fe/Mg/Al (10–7.5/40/42.5), (e) Co–Fe/Mg/Al (10–10/40/40), (f) Co–Fe/Mg/Al (10–12.5/40/37.5), (g) Co–Fe/Mg/Al (10–15/40/35) and (h) Fe/Mg/Al(10/50/40). (B) 8–14° regional XRD patterns, (C) 58–64° regional XRD patterns.

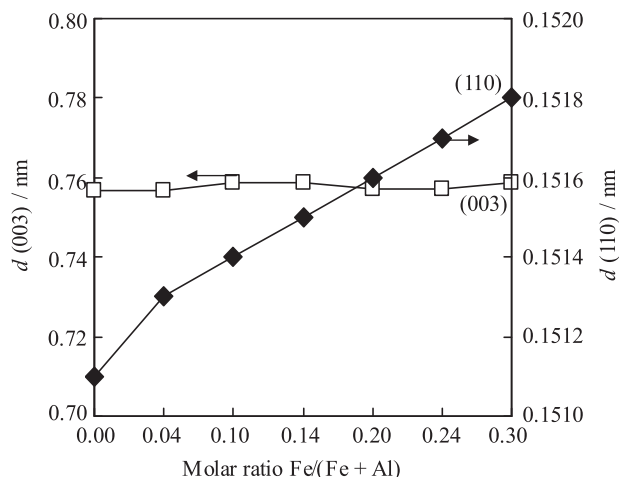


Fig. 2. Variation of XRD peak positions of the (003) and (110) reflections of as-synthesized samples as a function of Fe/(Fe + Al) molar ratio obtained from Fig. 1.

with the precursors of Co/Mg/Al (10/40/50) and Fe/Mg/Al (10/50/40). All XRD patterns exhibited the characteristic reflection peaks of hydrotalcite-like compounds [41] and no other peaks were observed, indicating the formation of a pure hydrotalcite phase in the precursors. The hydrotalcite-like structure, $[M^{2+}_{1-x}M^{3+}_x(OH)_2]^{x+}(CO_3)_{x/2} \cdot mH_2O$, consists of brucite-like sheets where M^{2+} and M^{3+} cations share octahedral positions, and interlayer CO_3^{2-} anions and water. The d -spacing of the (003) reflection at around $2\theta = 11^\circ$ corresponds to the thickness of one layer constituting a brucite-like sheet and one interlayer [46]. The d (003) values are plotted as a function of Fe/(Fe + Al) (Fig. 2), and they were almost constant (0.757–0.759 nm) for all the precursors (Fig. 2), suggesting that Fe^{3+} and Co^{2+} ions replace the

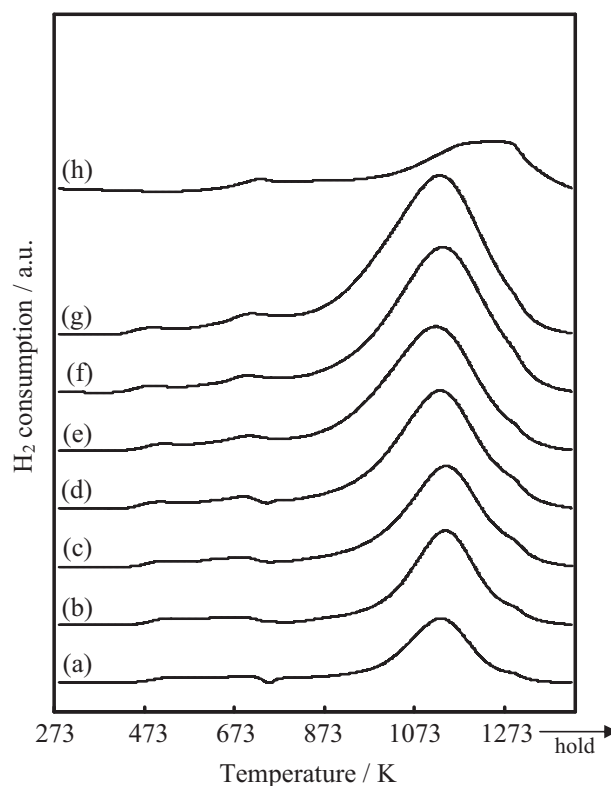


Fig. 4. TPR profiles of Co/Mg/Al, Fe/Mg/Al and Co-Fe/Mg/Al catalysts. (a) Co/Mg/Al(10/40/50), (b) Co-Fe/Mg/Al (10–2.5/40/47.5), (c) Co-Fe/Mg/Al (10–5/40/45), (d) Co-Fe/Mg/Al (10–7.5/40/42.5), (e) Co-Fe/Mg/Al (10–10/40/40), (f) Co-Fe/Mg/Al (10–12.5/40/37.5), (g) Co-Fe/Mg/Al (10–15/40/35) and (h) Fe/Mg/Al(10/50/40). TPR conditions: heating rate 10 K/min, 5% H₂/Ar flow rate 30 ml/min. Sample weight: 50 mg.

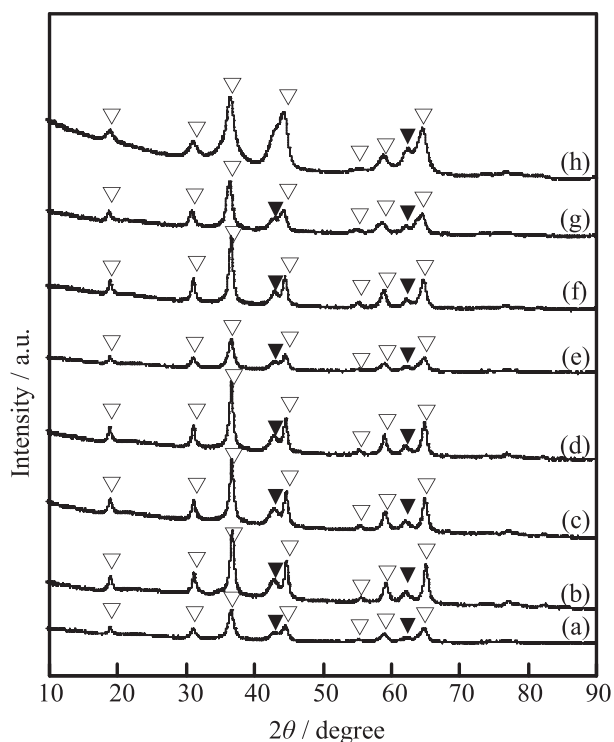


Fig. 3. XRD patterns of the samples after calcination: (a) Co/Mg/Al(10/40/50), (b) Co-Fe/Mg/Al (10–2.5/40/47.5), (c) Co-Fe/Mg/Al (10–5/40/45), (d) Co-Fe/Mg/Al (10–7.5/40/42.5), (e) Co-Fe/Mg/Al (10–10/40/40), (f) Co-Fe/Mg/Al (10–12.5/40/37.5), (g) Co-Fe/Mg/Al (10–15/40/35) and (h) Fe/Mg/Al(10/50/40). ▼ = MgO-based solid solution, ▽ = MgAl₂O₄-based solid solution.

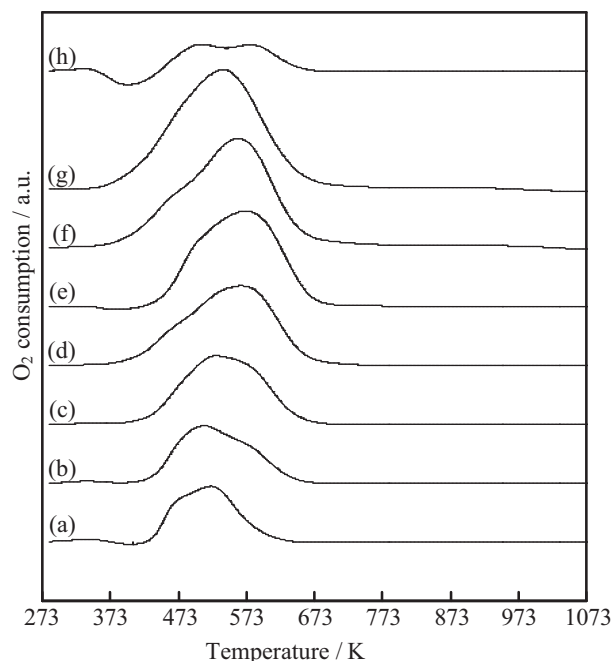


Fig. 5. TPO profiles of Co/Mg/Al, Co-Fe/Mg/Al and Fe/Mg/Al catalysts after the reduction pretreatment. (a) Co/Mg/Al(10/40/50), (b) Co-Fe/Mg/Al (10–2.5/40/47.5), (c) Co-Fe/Mg/Al (10–5/40/45), (d) Co-Fe/Mg/Al (10–7.5/40/42.5), (e) Co-Fe/Mg/Al (10–10/40/40), (f) Co-Fe/Mg/Al (10–12.5/40/37.5), (g) Co-Fe/Mg/Al (10–15/40/35) and (h) Fe/Mg/Al(10/50/40). TPO conditions: heating rate 10 K/min, 1% O₂/He flow rate 30 ml/min. Sample weight: 50 mg, condition of the reduction pretreatment: the fresh catalyst reduced at 1073 K in H₂/N₂ (1/1).

Al^{3+} and Mg^{2+} site, respectively. On the other hand, the d -spacing of the (1 1 0) reflection at around $2\theta = 61^\circ$ is related to the average metal ion–metal ion distance in the brucite-like sheet [46]. The d (1 0 0) values are also plotted as a function of $\text{Fe}/(\text{Fe} + \text{Al})$ (Fig. 2). The d (1 1 0) increased monotonously with increasing $\text{Fe}/(\text{Fe} + \text{Al})$. This can be explained by the partial replacement of Al^{3+} with Fe^{3+} cations in the hydrotalcite structure, because of the ionic radius of Fe^{3+} being larger than that of Al^{3+} (0.064 nm for Fe^{3+} and 0.054 nm for Al^{3+} in octahedral coordination) [47]. Totally, it is expected that Co^{2+} and Fe^{3+} cations are highly dispersed and homogeneously distributed at the Mg^{2+} and Al^{3+} sites in the brucite-like sheets, respectively.

Fig. 3 shows the XRD patterns of the Co–Fe/Mg/Al, Co/Mg/Al and Fe/Mg/Al after the calcination. On the Co–Fe/Mg/Al, Co/Mg/Al and Fe/Mg/Al catalysts, the characteristic XRD patterns assigned to hydrotalcite completely disappeared, and a diffraction pattern similar to that of MgAl_2O_4 -based solid solution [48] and MgO-based solid solution [49] was observed. The reduction pre-treatment of the calcined samples is essential for high catalytic performance in the steam gasification of biomass-derived tar. Therefore, H_2 -TPR was conducted to investigate the reduction behavior of the calcined samples. Fig. 4 shows the TPR profiles of the calcined samples of Co/Mg/Al, Co–Fe/Mg/Al and Fe/Mg/Al. For the Co/Mg/Al sample, the TPR profile exhibited a single reduction peak at ~ 1143 K, characteristic of the reduction of Co^{2+} species in both MgAl_2O_4 - and MgO-based solid solution [41]. Two reduction peaks at ~ 740 and 1200 K were observed for the Fe/Mg/Al sample, which might be attributed to the reduction of Fe^{3+} to Fe^{2+} and Fe^{2+} to α -Fe metal, respectively [37]. For Co–Fe/Mg/Al catalysts, TPR profiles showed a main peak at 1113–1125 K. The intensities of the main peak increased with increasing the Fe amount, suggesting the contribution of the reduction of Fe species. The small peak at ~ 740 K may be assigned to the reduction of surface Fe^{3+} to Fe^{2+} , and this

behavior supports that the peak at ~ 1125 K can be assigned to the co-reduction of Co and Fe. Based on the previous report on Ni/Mg/Al, the present reduction pretreatment was carried out at 1073 K, which was maintained for 0.5 h, in the stream of H_2/N_2 (30/30 ml/min) [50]. On the other hand, this temperature of 1073 K is located within the H_2 consumption peak in the TPR profiles and it is though that the reduction of Co and Fe species can proceed during the reduction pretreatment time (0.5 h). Therefore, it is not appropriate to determine the reduction degree of Co and Fe species from the results of TPR profiles. Here, we measured the TPO profiles of the catalysts after the same reduction pretreatment for the catalytic use.

Fig. 5 shows the TPO profiles of Co/Mg/Al, Co–Fe/Mg/Al and Fe/Mg/Al catalysts. The O_2 consumption is listed in Table 2. For Co/Mg/Al, the O_2 consumption peak due to the oxidation of Co metal gave a maximum at 530 K, where it is interpreted that Co metal particles are oxidized to Co_3O_4 according to the previous report [42]. On the other hand, O_2 consumption peak of Fe/Mg/Al is smaller than that of Co/Mg/Al, which is explained by higher oxygen affinity and lower reducibility of Fe than Co [39]. For all the Co–Fe/Mg/Al catalysts, the O_2 consumption increased from 1.42 to 3.52 mmol/g_{cat} with increasing the Fe content (Table 2, entries 2–6). It should be noted that this tendency essentially agreed with the order of the catalyst reducibility observed from TPR measurements (Fig. 4). In fact, the reduction degree determined by TPO profiles was clearly higher than that from the amount of H_2 consumption below the pretreatment reduction temperature of 1073 K, and this indicates that the reduction of Co and Fe species proceed during the reduction pretreatment time (0.5 h).

Fig. 6 shows the XRD patterns of Co/Mg/Al, Fe/Mg/Al and Co–Fe/Mg/Al catalysts after the reduction pretreatment. The peak at $2\theta \equiv 51.5^\circ$ on Co/Mg/Al was small (Fig. 6A(a)), however, it has been verified in Fig. 6B(a) that the peak is assigned to Co metal

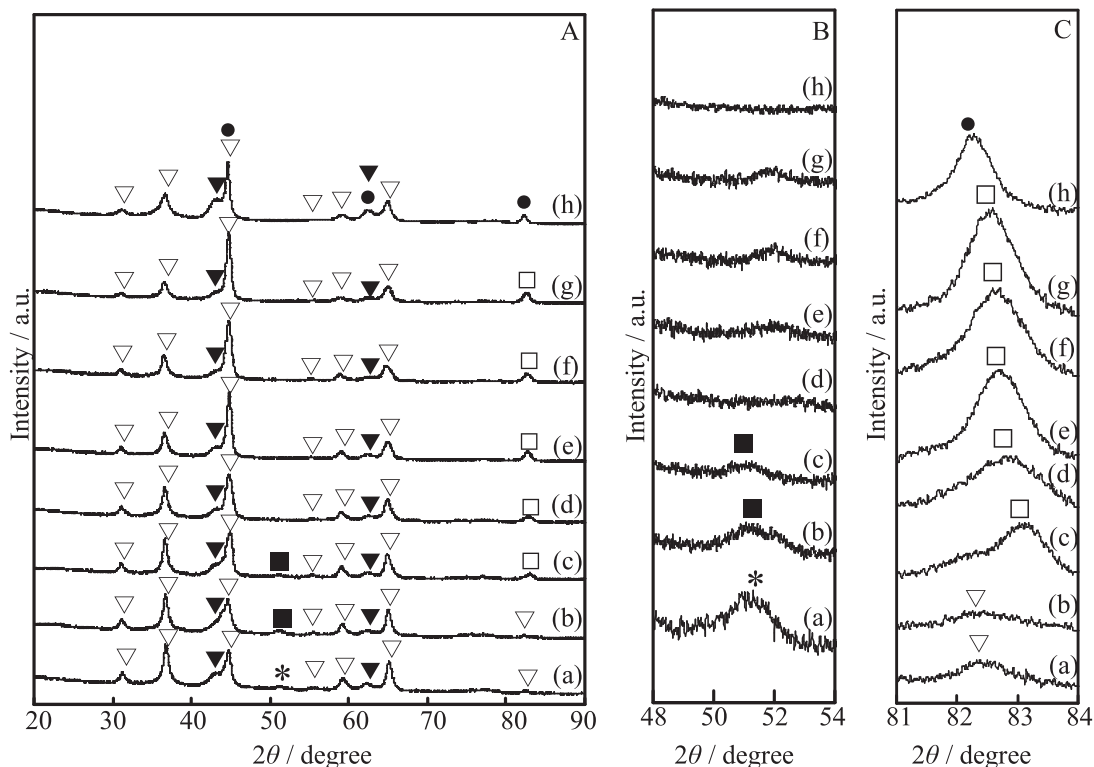


Fig. 6. (A) XRD patterns of the samples after the reduction pretreatment. (a) Co/Mg/Al (10–40/50), (b) Co–Fe/Mg/Al (10–2.5/40/47.5), (c) Co–Fe/Mg/Al (10–5/40/45), (d) Co–Fe/Mg/Al (10–7.5/40/42.5), (e) Co–Fe/Mg/Al (10–10/40/40), (f) Co–Fe/Mg/Al (10–12.5/40/37.5), (g) Co–Fe/Mg/Al (10–15/40/35) and (h) Fe/Mg/Al (10/50/40) ∇ = MgO-based solid solution, ∇ = MgAl_2O_4 -based solid solution, \bullet = Fe metal, $*$ = Co metal, \blacksquare = Co–Fe fcc alloy and \square = Co–Fe bcc alloy. (B) 48–54° regional XRD patterns, (C) 81–84° regional XRD patterns.

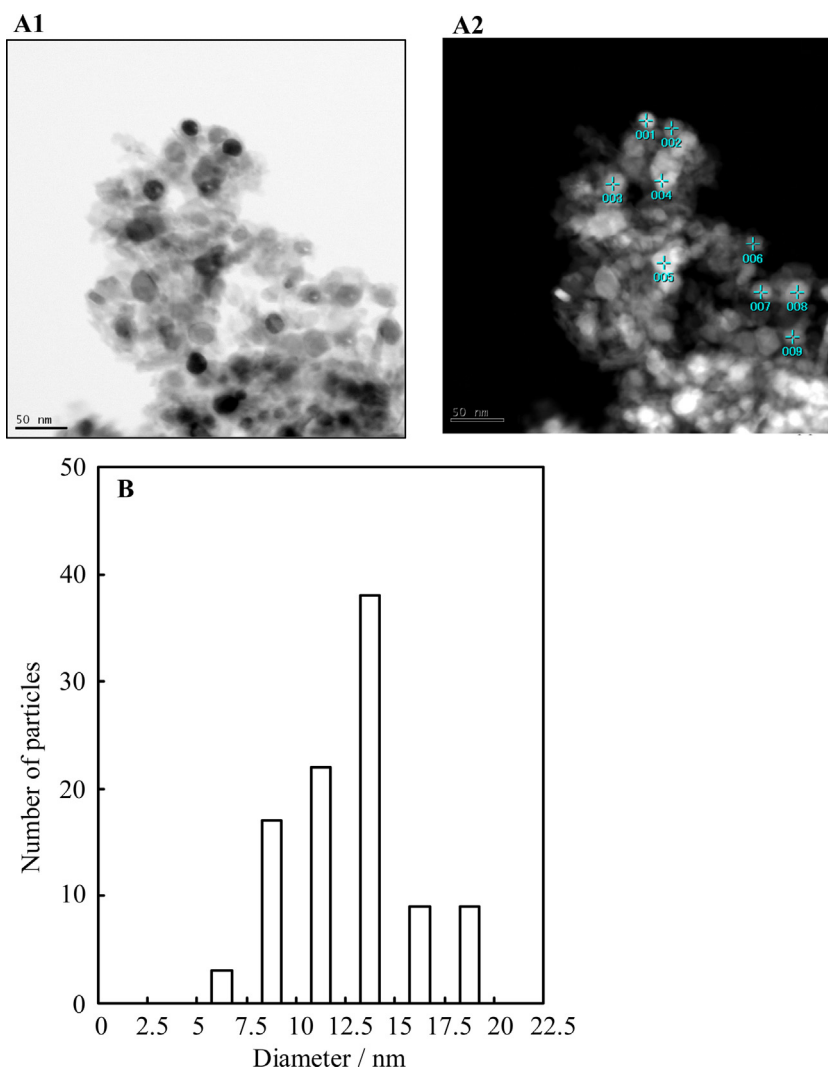
Table 2
Properties of prepared catalysts.

Entry	Catalysts	Content (mmol/g)		O ₂ consumption in TPO (mmol/g _{cat}) ^a	Reduction degree (%) ^b	H ₂ adsorption (10 ^{−6} mol/g) ^c	Dispersion (%) ^d
		Co	Fe				
1	Co/Mg/Al (10/40/50)	2.04	–	1.10	81	32	3.90
2	Co–Fe/Mg/Al (10–2.5/40/47.5)	2.04	0.51	1.42	84	3.2	0.30
3	Co–Fe/Mg/Al (10–5/40/45)	2.04	1.02	1.76	86	4.5	0.34
4	Co–Fe/Mg/Al (10–7.5/40/42.5)	2.04	1.53	2.26	95	4.7	0.28
5	Co–Fe/Mg/Al (10–10/40/40)	2.04	2.04	2.44	90	7.7	0.42
6	Co–Fe/Mg/Al (10–12.5/40/37.5)	2.04	2.55	3.12	102	6.6	0.28
7	Co–Fe/Mg/Al (10–15/40/35)	2.04	3.05	3.52	104	6.1	0.23
8	Fe/Mg/Al (10/50/40)	–	2.08	0.61	44	1.1	0.24

^a Calculated from the temperature programmed oxidation measurement of the reduced catalysts (Fig. 5).^b Reduction degree = [O₂ consumption in TPO]/([Co] × 2/3 + [Fe] × 2/3).^c The total adsorption (Irreversible + Reversible) at room temperature on the catalysts after reduction.^d Dispersion = 2 × [H₂ adsorption]/[O₂ consumption].

with fcc structure ((200) plane) as reported previously [41], and the peak due to Fe metal with bcc structure was observed at $2\theta \equiv 82.23^\circ$ ((211) plane) on Fe/Mg/Al. In the case of Co–Fe/Mg/Al (10–2.5/40/47.5 and 10–5/40/45), the peak were located around at $2\theta \equiv 51.3^\circ$ – 51.5° as shown in Fig. 6B(b) and (c), respectively. The position of the peaks shifted to smaller diffraction angle and they seem to approach the reported position due to fcc Fe

metal ($2\theta \equiv 49.99^\circ$ [51]) slightly with increasing the amount of Fe addition. Therefore, it can be interpreted that the peak at 51.3° – 51.5° can be assigned to Co–Fe fcc alloy, where Fe atoms substitute Co sites in fcc structure of Co metal to give the solid solution. This phase disappeared on the samples of Co–Fe/Mg/Al (10– x /40/(50– x), $x \geq 7.5$) as shown in Fig. 6B(d–g). On the other hand, the peak around at $2\theta \equiv 83^\circ$ grew significantly on the

**Fig. 7.** TEM image of the Co–Fe/Mg/Al (10–10/40/40) (A) and the distribution of the size of Co–Fe alloy particles (B) after H₂ pretreatment at 1073 K.

samples of Co–Fe/Mg/Al (10– x /40/(50– x), $x \geq 7.5$) as shown in Fig. 6C. According to the previous report [19], the (2 1 1) diffraction angle of bcc Co metal (the lattice constant: 0.2827 nm [52]) is calculated to be $2\theta \equiv 83.67^\circ$, and the observed peaks on Co–Fe/Mg/Al (10–5/40/47.5–10–15/40/35 (Fig. 6C(c–g)) are located between the peaks due to bcc Co and bcc Fe metals, and the position of the peaks shifted to lower diffraction angle gradually with increasing Fe amount. This tendency indicates the formation of Co–Fe bcc alloy, where Co atoms substitute Fe sites in bcc structure of Fe metal to give the solid solution. In addition, the structure of the Co–Fe bcc alloy (Co/Fe=1/1) has been reported and the (2 1 1) diffraction angle of this compound was observed at $2\theta \equiv 82.78^\circ$ [53]. This also supports the Co–Fe bcc alloy formation. An important point is that the Co–Fe bcc alloy has high potential in the steam reforming reaction [23]. Another important point is that both Co–Fe fcc and bcc alloy phases were simultaneously formed on Co–Fe/ α -Al₂O₃ [19], in contrast, only the bcc Co–Fe

alloy phase was formed on Co–Fe/Mg/Al (Fe/Co > 0.25, Fig. 6B and C(c–g)).

Fig. 7 shows the STEM image of Co–Fe/Mg/Al (10–10/40/40) and the size distribution of metal particles. Since the metal particles give higher contrast than oxides, metal particles can be observed as the dark and bright parts in Fig. 7A1 and A2, respectively. It should be noted that the reduction degree of Co and Fe species was 90% (Table 2, Entry 5) on the reduced Co–Fe/Mg/Al (10–10/40/40) and unreduced Co and Fe species are located in the oxides mainly consisting of Mg and Al, which cannot be observed in the TEM images. The size distribution of metal particles was determined only from the metallic Co and Fe species formed by the reduction. The average size of metal particles was calculated to be 14 nm. The elemental composition of the various positions on the Co–Fe/Mg/Al (10–10/40/40) was measured by the EDX analysis as listed in Table 3. The molar ratio of Fe/Co obtained from the EDX analysis was in the range of 0.3–1.8. One of the most

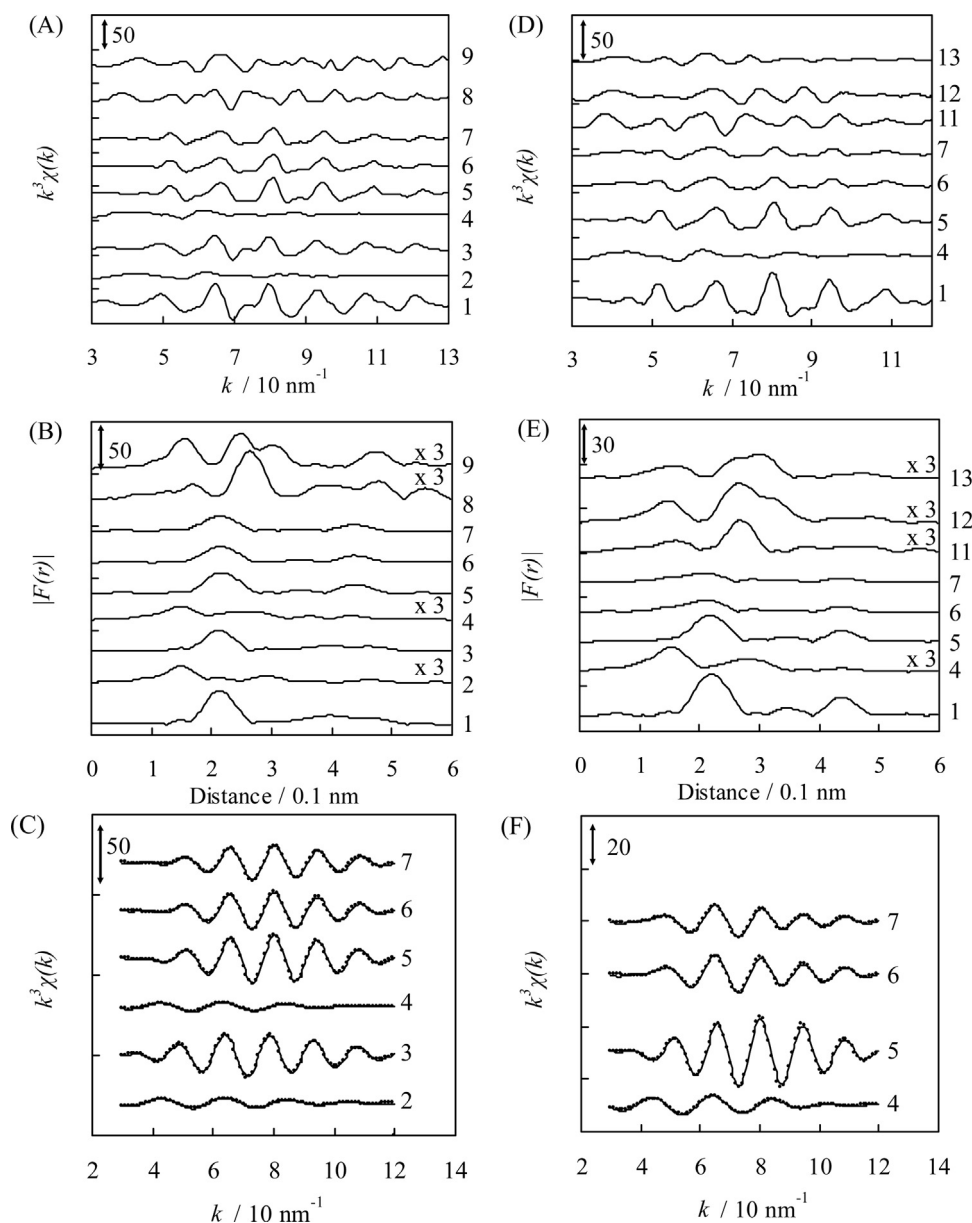


Fig. 8. Results of EXAFS analysis of Co–Fe/Mg/Al (10–10/40/40) and Co/Mg/Al (10/40/50). (1) Co foil, (2) Co/Mg/Al after the calcination, (3) Co/Mg/Al after the reduction, (4) Co–Fe/Mg/Al after the calcination, (5) Co–Fe/Mg/Al after the reduction, (6) Co–Fe/Mg/Al after the reaction (Fig. 11A), (7) Co–Fe/Mg/Al after the reaction (Fig. 11C), (8) CoO, (9) Co₃O₄, (10) Fe foil, (11) FeO, (12) Fe₂O₃, (13) Fe₃O₄. (A)–(C): Co K-edge, (D)–(F): Fe K-edge, (A) and (D): k^3 -weighted EXAFS oscillation. (B) and (E): Fourier transform of k^3 -weighted EXAFS, FT range: 30–120 nm^{−1}. (C) and (F): Fourier filtered EXAFS data (solid line) and calculated data (dotted line).

important points is that the simultaneous presence of Co and Fe species in all the respective particles was verified, and this supports the Co–Fe alloy formation. This behavior cannot be explained by Co and Fe species in the oxides because the amount was much smaller than that of Co and Fe species in metal particles. On the other hand, the composition of each particle is not so uniform as the case of Ni–Fe/Mg/Al [37], although the distribution of the composition is narrower than the case of Co–Fe/ α -Al₂O₃ [19]. It should be noted that the average of the composition of nine points is calculated to be Fe/Co = 0.9. As a reference, we calculated the average size of the Co–Fe bcc alloy particle on Co–Fe/Mg/Al using Scherrer equation [54] (Fig. 7B) assuming the uniform composition. The obtained value is 7 nm, which is smaller than that from STEM observation. This inconsistency can be explained by the degree of the inhomogeneity in the composition of each alloy particles as listed in Table 3.

The Co–Fe/Mg/Al (10–10/40/40) catalyst was also characterized by Co *K*-edge and Fe *K*-edge EXAFS comparing to Co/Mg/Al (10/40/50), and Fig. 8 shows EXAFS results of Co/Mg/Al (10/40/50) and Co–Fe/Mg/Al (10–10/40/40) after the calcination and the reduction pretreatment together with those of reference compounds. The curve fitting results are listed in Tables 4 and 5. In the EXAFS analysis of Co/Mg/Al (10/40/50), the spectrum of the calcined sample was fitted with two Co–O bonds, i.e., tetrahedral Co–O with the bond distance (*R*) of 0.185 nm (cf. in normal spinel CoAl₂O₄: 0.196 nm [55]) and octahedral Co–O (*R* = 0.201 nm) (cf. in inverse spinel CoAl₂O₄: 0.206 nm [55]). It is characteristic that the FT spectrum of Co/Mg/Al (10/40/50) (Fig. 8B) gave much

Table 3

Results of energy-dispersive X-ray analysis of the Co–Fe/Mg/Al (10–10/40/40) after the H₂ reduction at 1073 K.

Position in Fig. 7A2	Relative signal intensity		Molar ratio Fe/Co
	Co	Fe	
1	0.48	0.52	1.1
2	0.48	0.52	1.1
3	0.63	0.37	0.6
4	0.54	0.46	0.8
5	0.63	0.37	0.6
6	0.65	0.35	0.5
7	0.77	0.23	0.3
8	0.36	0.64	1.8
9	0.40	0.60	1.5

smaller peak in *R* range of 0.22–0.35 nm than that of CoO and Co₃O₄. This suggests that the Co species did not form CoO or Co₃O₄, and the species were dispersed in MgO and MgAl₂O₄ structure. The weak FT band in the range of *R* = 0.22–0.35 nm can be explained by a variety of states, for example, Mg²⁺ or Al³⁺ sites in MgO and MgAl₂O₄. After the reduction, the contribution of the Co–O bonds decreased and that of the Co–Co bond increased drastically. The residual Co–O bond indicates that the Co species are not reduced completely, which is also supported by the reduction degree listed in Table 2. Judging from the particle size of Co metal (14 nm) [41], the smaller CN of Co–Co (9.6) than that of bulk Co metal (12) can be explained by the presence of this unreduced Co species. This

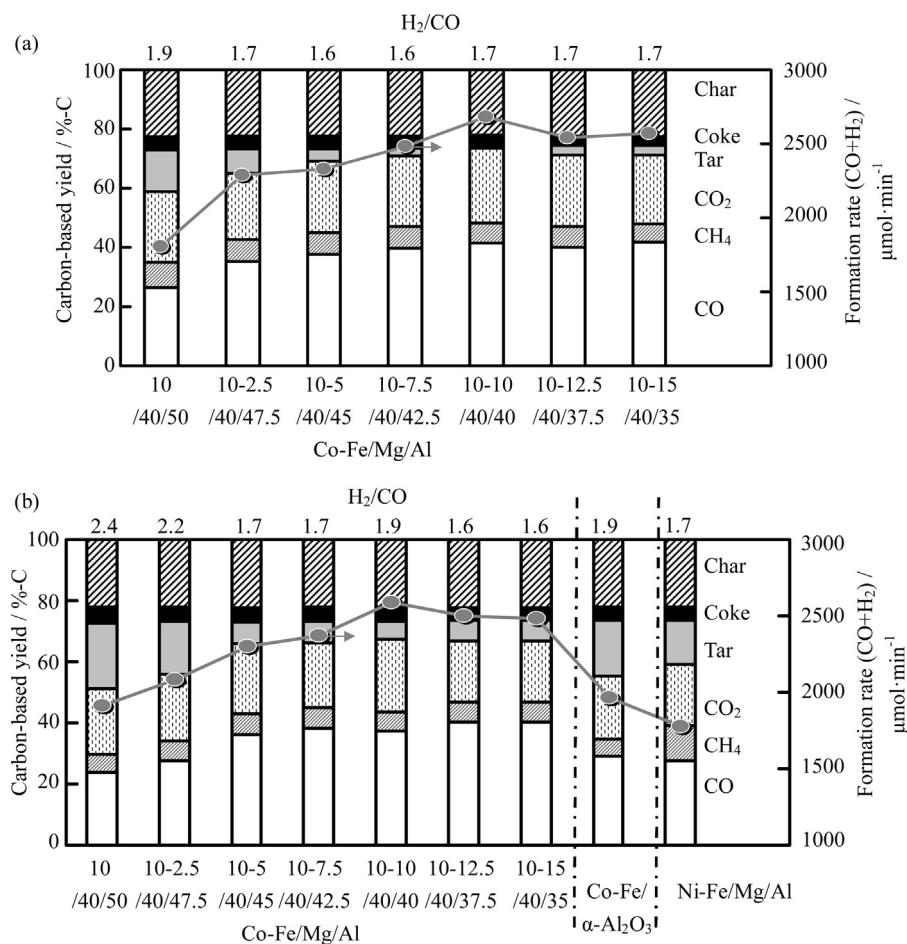


Fig. 9. Catalytic performance in the steam gasification of biomass-derived tar over Co–Fe/Mg/Al and reference catalysts at 823 K. Catalyst weight was 0.3 g, (a): S/C = 0.38, (b): S/C = 0.23.

Table 4Curve fitting results of Co *K*-edge EXAFS of Co/Mg/Al (10/40/50) and Co-Fe/Mg/Al (10–10/40/40) after the calcination and the reduction.

Catalyst	Treatment	FF range ^a (10 ^{−1} nm)	Shells	CN ^b	<i>R</i> (10 ^{−1} nm) ^c	σ (10 ^{−1} nm) ^d	ΔE_0 (eV) ^e	<i>R_f</i> (%) ^f
Co/Mg/Al	Calcination	1.044–1.964	Co–O	2.5	1.85	0.062	−9.2	0.6
			Co–O	3.5	2.01	0.063	−2.0	
Co/Mg/Al	Reduction	1.166–2.639	Co–O	1.2	1.95	0.070	−3.1	0.6
			Co–Co	9.6	2.50	0.075	−1.8	
Co-Fe/Mg/Al	Calcination	1.044–1.964	Co–O	2.6	1.87	0.062	−9.2	0.5
			Co–O	3.3	2.03	0.063	−2.6	
Co-Fe/Mg/Al	Reduction	1.258–2.762	Co–O	0.7	1.97	0.075	6.9	0.7
			Co–Fe (or Co)	7.2	2.48	0.066	−0.1	
Co foil			Co–Fe (or Co)	5.4	2.86	0.075	2.0	–
			Co–Co	12.0	2.51	0.060	0	
NiO			Ni–O	6.0	2.09	0.060	0	–

^a Fourier filtering range.^b Coordination number.^c Bond distance.^d Debye–Waller factor.^e Difference in the origin of photoelectron energy between the reference and the sample.^f Residual factor. Co: 12 wt%, Fe/Co = 1.

behavior can be verified from the XANES analysis (Fig. S1). The area of the first peak of Co/Mg/Al (10/40/50) is between that of Co foil and Co oxides.

In the case of Co *K*-edge EXAFS of Co-Fe/Mg/Al (10–10/40/40) after the calcination (Fig. 8(4), Table 4), the spectrum and the curve fitting results are similar to those of Co/Mg/Al (10/40/50), indicating that the local structure of the Co species after the calcination is almost the same on Co/Mg/Al (10/40/50) and Co-Fe/Mg/Al (10–10/40/40). In the case of Co *K*-edge EXAFS analysis of Co-Fe/Mg/Al (10–10/40/40) after the reduction, two different Co–Co (or Fe) bonds were applied to the curve fitting analysis judging from the XRD results indicating that the main phase of metallic species is Co–Fe bcc alloy. The analysis based on the bcc phase is also supported by the shape in the FT spectrum at $R \geq 0.3$ nm. The shape in this range is very sensitive to the crystal structure of fcc (Co foil) (Fig. 8(1)) and bcc (Fe foil) (Fig. 8(10)). The shape of Co-Fe/Mg/Al (10–10/40/50) (Fig. 8(4)) is clearly similar to that of bcc (Fe foil) structure. In addition, the CN of the Co–O bond on Co-Fe/Mg/Al (10–10/40/40) after the reduction is a little smaller than that on Co/Mg/Al (10/40/50) and this is also supported by the H₂ consumption amount in Table 2. Totally, the good fitting with Co–O and two Co–Fe (or Co) bonds regarding Co-Fe/Mg/Al (10–10/40/40) was obtained. The CN of two Co–Fe (or Co) bonds (7.2 and 5.4) were close to those (8 and 6) in the bcc structure (Fe foil in Table 5), which can be interpreted by high reduction of Co on Co-Fe/Mg/Al (10–10/40/40). As a result, an important point is that monometallic Co metal particle tends to give fcc structure, and the incorporation of Co atoms to bcc structure can be due to the alloy formation with Fe. Another important point is

that the reduction degree of Co is promoted by the presence of Fe.

Regarding Fe *K*-edge EXAFS analysis, at first, the curve fitting analysis of Fe foil using the phase shift and the backscattering amplitude functions extracted from Co foil was carried out in order to check the validity of this analysis method (Table 5). In the case of Co-Fe/Mg/Al after the calcination, two kinds of Fe–O bond were detected and they are interpreted by tetrahedral and octahedral Fe ion species like the case of Co species after the calcination. After the reduction, the contribution of Fe–O bond was negligible, and the Fe–Fe (–or Co) bonds were observed. The bond distance and CN of two Fe–Fe (–or Co) bonds on Co-Fe/Mg/Al (10–10/40/40) after the reduction were very similar to those on Fe foil. This indicates that Fe atoms are mainly incorporated into bcc structure and the formation of Co–Fe bcc alloy can explain the behavior of bond distance and CN. In addition, the reduction degree regarding Fe can be rather high, which is also supported by Fe *K*-edge XANES analysis (Fig. S2).

The amount of H₂ adsorption was measured and the results are also listed in Table 2. The addition of small amount of Fe decreased H₂ adsorption amount drastically. In the case of Co-Fe/Mg/Al (10–10/40/40), the O₂ consumption amount of TPO was 2.44 mmol/g_{cat}, and the reduction degree of Co + Fe is calculated to be 0.9 (Table 2, entry 5). This suggests that almost all the Co and Fe species are reduced to the metallic state. On the other hand, the relation between particle size of Fe metal particles and the dispersion has been reported [56], and the particle size of 14 nm gives 5.4% dispersion using ($d = 0.75/D$; *D*: dispersion, *d*/nm: particle size) [56]. In fact, the dispersion obtained from H₂ adsorption amount on Co-Fe/Mg/Al (10–10/40/40) is calculated to be 0.42%

Table 5Curve fitting results of Fe *K*-edge EXAFS of Co-Fe/Mg/Al (10–10/40/40) after the calcination and the reduction.

Catalyst	Treatment	FF range ^a (10 ^{−1} nm)	Shells	CN ^b	<i>R</i> (10 ^{−1} nm) ^c	σ (10 ^{−1} nm) ^d	ΔE_0 (eV) ^e	<i>R_f</i> (%) ^f
Fe foil		1.596–2.823	Fe–Fe	8.0	2.48	0.060	0.5	0.7
			Fe–Fe	6.0	2.87	0.060	0.5	
Co-Fe/Mg/Al	Calcination	1.044–2.056	Fe–O	2.4	1.86	0.060	−9.7	1.4
			Fe–O	3.6	2.04	0.060	6.4	
Co-Fe/Mg/Al	Reduction	1.596–2.700	Fe–Co (or Fe)	7.8	2.48	0.073	0.6	0.6
			Fe–Co (or Fe)	5.9	2.87	0.078	6.0	
NiO			Ni–O	6.0	2.09	0.060	0.0	–
			Co–Co	12.0	2.51	0.060	0.0	

^a Fourier filtering range.^b Coordination number.^c Bond distance.^d Debye–Waller factor.^e Difference in the origin of photoelectron energy between the reference and the sample.^f Residual factor. Co: 12 wt%, Fe/Co = 1.

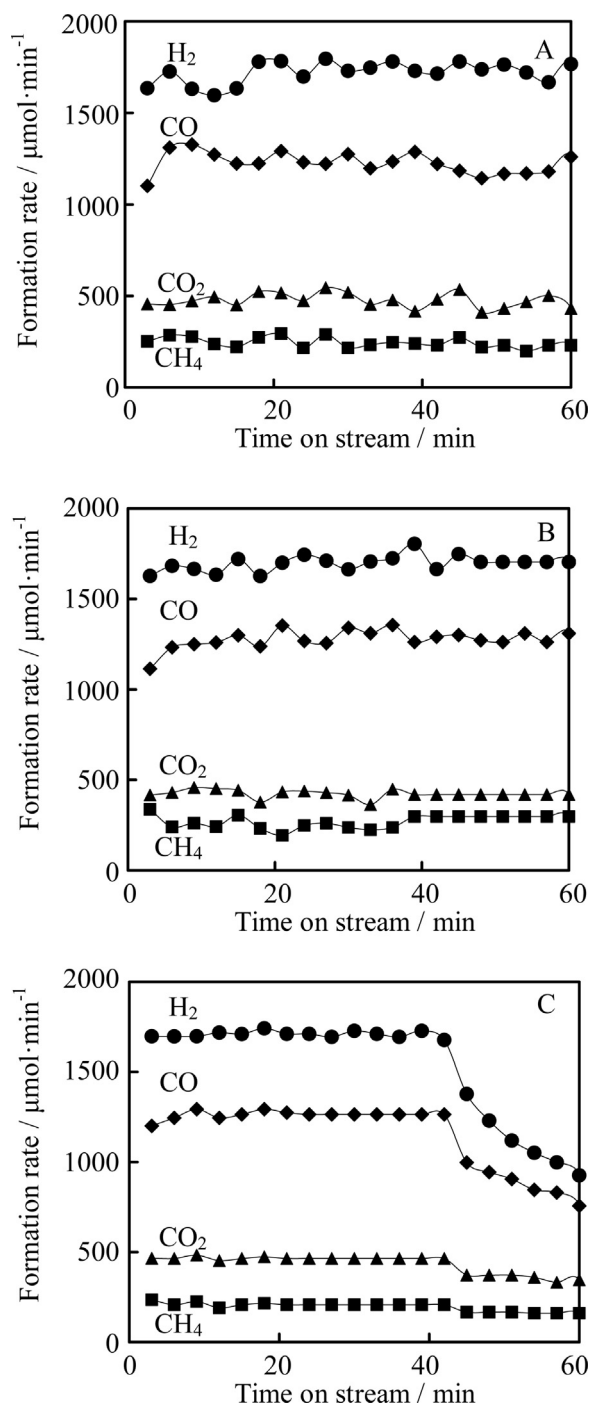


Fig. 10. Reaction time dependence of steam gasification of biomass-derived tar over Co-Fe/Mg/Al (10–10/40/40) at 873 K and $S/C=0.23$. Catalyst weight was 0.3 g. (A) The fresh catalyst reduced at 1073 K in H_2/N_2 (1/1). (B) The used catalyst of (A) after the oxidation with O_2/N_2 (1/3) at 873 K for 1 h and the subsequent reduction at 1073 K in H_2/N_2 (1/1). (C) The used catalyst of (B) after the oxidation with O_2/N_2 (1/3) at 873 K for 1 h and the subsequent reduction at 1073 K in H_2/N_2 (1/1).

(Table 2, entry 5), which is much smaller than that from the particle size. Based on this discussion, it is thought that the Co-Fe bcc alloy formation can suppress the H_2 adsorption strongly.

3.2. Catalytic performance of Co-Fe/Mg/Al in the steam gasification of biomass-derived tar

Fig. 9a shows the catalytic performance of Co/Mg/Al and Co-Fe/Mg/Al in steam gasification of biomass-derived tar at 823 K

and $S/C=0.38$. In the case of Co/Mg/Al, the amount of the residual tar was large and the formation rate of $CO+H_2$ was rather low, indicating the low catalytic activity of Co/Mg/Al in the steam reforming reaction of tar derived from the pyrolysis of cedar wood. On the other hand, the addition of Fe to Co/Mg/Al decreased the amount of tar and increased the formation rate of $CO+H_2$. In addition, we have already reported that monometallic Fe catalysts such as Fe/Mg/Al and Fe/ $\alpha-Al_2O_3$ had much lower activity than Co/Mg/Al and Co/ $\alpha-Al_2O_3$ catalysts under similar reaction conditions in the steam gasification of biomass-derived tar [14,19,37]. The optimum composition is determined to be Co-Fe/Mg/Al = 10–10/40/40. However, the optimized catalyst gave almost no tar formation at $S/C=0.38$, and it is difficult to compare the catalysts from the viewpoint of the catalytic activity. Therefore, we also tested at $S/C=0.23$, which is severer conditions than $S/C=0.38$. In addition, the performance of Co-Fe/Mg/Al was compared with Co-Fe/ $\alpha-Al_2O_3$ and Ni-Fe/Mg/Al (9.1–2.3/66/22.6), which have been optimized in our previous works [19,37].

Fig. 9(b) shows that Co-Fe/ $\alpha-Al_2O_3$ exhibited very low activity, under the present reaction condition, in contrast, hydrotalcite-derived catalysts (Co/Mg/Al and Co-Fe/Mg/Al) showed higher activity than Co-Fe/ $\alpha-Al_2O_3$. On the other hand, catalyst properties of the Co-Fe/Mg/Al and Co-Fe/ $\alpha-Al_2O_3$ catalysts are compared [19]. The loading amount of Co was almost the same on both catalysts. Reduction degree of Co and Fe species on Co-Fe/ $\alpha-Al_2O_3$ was comparable to that of Co-Fe/Mg/Al [19]. Average particle size of Co-Fe/ $\alpha-Al_2O_3$ was determined to be 28 nm, which were smaller than that of Co-Fe/Mg/Al [19]. On both catalysts, the average metal particle size is rather large, and this suggests that the contribution of the support oxide to the catalytic activity is small. As a result, the higher activity of Co-Fe/Mg/Al than that of Co-Fe/ $\alpha-Al_2O_3$ can be due to smaller metal particle size and the property of metal particles such as the composition and its uniformity. It should be noted that Co-Fe/ $\alpha-Al_2O_3$ (Fe/Co = 1) showed much lower activity than Co-Fe/ $\alpha-Al_2O_3$ (Fe/Co = 0.25) [19]. Similar tendency has been also observed in the previous results on Ni-Fe/ $\alpha-Al_2O_3$, Ni/Mg/Al, and Ni-Fe/Mg/Al [37,50].

An interesting point is that Co-Fe/Mg/Al catalysts have higher activity than Co/Mg/Al (10–10/40/50) regardless of much smaller H_2 adsorption amount (Table 2). The H_2 adsorption amount on the reduced catalyst gave complicated dependence of Fe content and this suggests that the H_2 adsorption amount is influenced by not only the number of surface metal atoms but also various factors such as metal structure (fcc and bcc) and surface composition of the alloys. It is characteristic that Co-Fe/Mg/Al (10–2.5/40/47.5) has very small amount of H_2 adsorption (Table 2, entry 2). According to XRD analysis, the fcc Co-Fe alloy formation was suggested, which may be connected to small H_2 adsorption amount, for example, caused by the surface segregation of Fe species on the fcc alloy particles. The bcc Co-Fe alloy tends to be formed with increasing Fe content, and this can be connected to the increase of H_2 adsorption amount. On the other hand, the increase of Fe content in the bcc alloy phase can decrease the H_2 adsorption amount. As a result, it is thought that the H_2 adsorption amount became the maximum on Co-Fe/Mg/Al (10–10/40/40). This behavior can be related to high catalytic activity in the steam gasification of biomass-derived tar from the viewpoint that the sites having the ability of H_2 dissociation and adsorption can play an important role on the dissociation of C–H and C–C bonds in the biomass-derived tar compounds. Here, the catalytic performance of Co-Fe/Mg/Al (10–10/40/40) was compared with that of the optimized Ni-Fe/Mg/Al (9.1–2.3/66/22.6) in our previous work [37], it is concluded that Co-Fe/Mg/Al (10–10/40/40) exhibited higher catalytic activity than Ni-Fe/Mg/Al (9.1–2.3/66/22.6). The H_2 adsorption amount of Ni-Fe/Mg/Al (9.1–2.3/66/22.6) was determined to be $38.9 \mu\text{mol/g}_{\text{cat}}$ [37], which was larger than that of

Co-Fe/Mg/Al (10–10/40/40) (Table 2, entry 5). Considering from the H_2 adsorption amount, Co-Fe/Mg/Al was especially superior to Ni-Fe/Mg/Al for the steam gasification of biomass-derived tar, and the same trend has been also reported on Co-Fe/ α - Al_2O_3 and Ni-Fe/ α - Al_2O_3 [14,19]. These behaviors are connected to the high potential of the bcc Co-Fe alloy phase as an active species compared to the fcc Ni-Fe alloy phase. In addition, we also compared the catalytic performance of Co/Mg/Al (10/40/50), Co-Fe/Mg/Al (10–10/40/40) and Ni/Mg/Al (9.1–2.3/66/22.6) at different reaction temperatures (Fig. S3). Co-Fe/Mg/Al (10–10/40/40) showed highest activity in the steam gasification of biomass-derived tar among these three catalysts. In particular, the activity of Co-Fe/Mg/Al (10–10/40/40) at 823 K was higher than that of Co/Mg/Al (10/40/50) at 873 K, indicating the addition of Fe to Co/Mg/Al (10/40/50) can decrease the reaction temperature by 50 K.

3.3. Catalyst regeneration test and characterization

It has been known that catalysts can be deactivated by the coke deposition [57–61] and structural change such as the aggregation

of metal particles [57] in the reforming reaction. The deactivation becomes severer when the partial pressure ratio of steam to carbon is lower. However, the suppression of coke deposition by higher partial pressure of steam than the reaction stoichiometry decreased the energy efficiency of the steam gasification reaction. One possible method for the energy-efficient steam gasification with an appropriate partial pressure of steam is the development of catalysts with higher resistance to coke deposition. However, it is very difficult to suppress the coke formation completely. The regeneration of the used catalyst by the removal of the deposited coke with the combustion is an important property [62,63], in particular, in terms of the practical view.

In order to evaluate the deactivation behavior and the regeneration ability, the activity test was carried out at low steam to carbon ratio ($S/C=0.23$). Fig. 10 shows the results of the repeated use of Co-Fe/Mg/Al (10–10/40/40) in the steam gasification. Even at low S/C conditions, Co-Fe/Mg/Al (10–10/40/40) maintained high activity of the steam gasification. However, at third use, the activity decreased drastically. As shown in Fig. S3, the amount of residual tar was negligible at 873 K, indicating that the catalyst amount

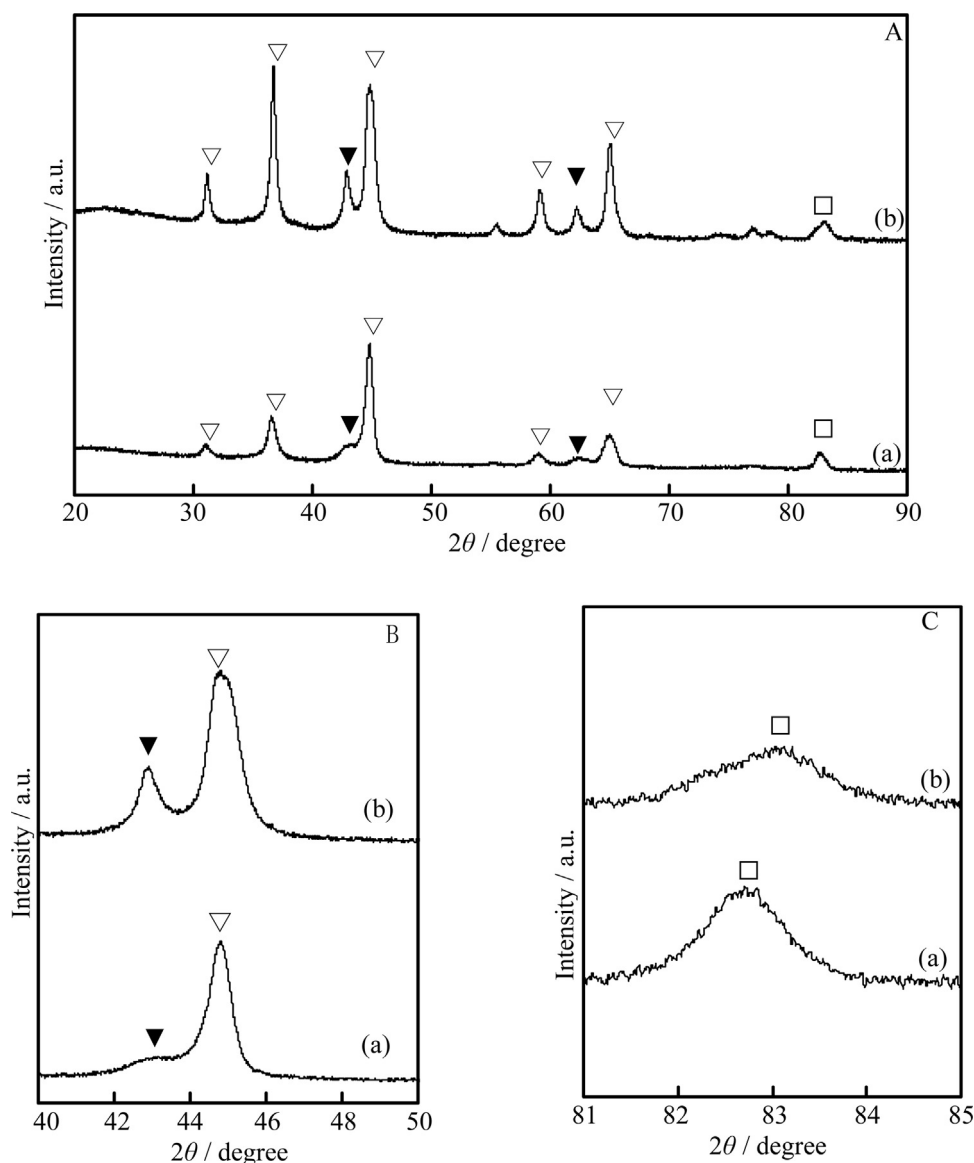


Fig. 11. XRD patterns (A, B and C) of the Co-Fe/Mg/Al (10–10/40/40) after the reduction pretreatment (a) and the catalytic use (b) (Fig. 10C). ▽ = MgO-based solid solution, ▴ = $MgAl_2O_4$ -based solid solution and □ = Co-Fe bcc alloy.

needed for the complete conversion of tar is much less than 0.3 g. Therefore, at first and second use, the constant formation rate of the products was observed, although the catalytic activity can be decreased gradually. It is interpreted that the catalytic activity at third use can be decreased first by the regeneration treatment and then the decrease of the activity during the reaction became obvious. As a result, it is concluded that the steam gasification activity of Co–Fe/Mg/Al (10–10/40/40) gradually decreased by the repeated times. It should be noted that the amount of deposited coke was 3.1 mmol/g_{cat} after 60 min (Fig. 10C) at 873 K. On the other hand, the amount of coke was 4.6 mmol/g_{cat} after 15 min in Fig. 8b at 823 K (2.7 mmol/g_{cat} after 15 min in Fig. S3 at 873 K). The amounts were not so different, and this indicates that the main cause of the deactivation is not the coke deposition. In order to elucidate the cause of the deactivation, the used catalyst was also characterized.

Fig. 11 shows the XRD patterns of Co–Fe/Mg/Al (10–10/40/40) after the reduction pretreatment and the catalytic use. It is characteristic that the peak around $2\theta = 43^\circ$ due to MgO-based solid solution grew by the catalytic use, suggesting that the repeated use changed the structure of oxides to give MgO-based solid solution. At the same time, it is characteristic that the peak around $2\theta = 82.6^\circ$ due to the Co–Fe bcc alloy phase shifted to higher angle and the peak intensity was decreased. This behavior can be interpreted by the oxidation of the Co–Fe bcc alloy phase, in particular, the selective oxidation of Fe species, which cause the decrease of Fe content in the alloy phase and molar ratio of Fe/Co.

Fig. 8 also shows Co and Fe K-edge EXAFS spectra of Co–Fe/Mg/Al (10–10/40/40) after the catalytic use. The results of the curve fitting analysis are listed in Table 6. From the curve fitting analysis of Co K-edge EXAFS, the catalytic use increased gradually the CN of Co–O, in contrast, decreased the CN of Co–Co (–or Fe). This can be explained by the oxidation of Co species in the bcc Co–Fe alloy phase. On the other hand, the increase of the CN of two Fe–O bonds and the decrease of the CN of two Fe–Fe (–or Co) bonds in the Fe K-edge EXAFS analysis were much more significant than those in the Co K-edge EXAFS analysis. This indicates that the Fe species in the bcc Co–Fe alloy phase tends to be more easily oxidized than the Co species, which is connected to the peak shift to higher angle of the Co–Fe alloy phase (Fig. 11) indicating the decrease of Fe/Co in the unoxidized alloy phase. In addition, the width of the XRD peak ($2\theta = 83^\circ$) did not become narrower after the catalytic use, indicating that aggregation of metal particles did not proceed. Considering the relation between the structural change of the catalyst after the catalytic use and the activity trend in the repeated use, it is suggested that Co–Fe bcc alloy particles on MgO-based solid solution are oxidized more easily than those on MgAl₂O₄-based solid solution as discussed below.

Fig. 12 shows the results of the repeated use of the Co–Fe/ α -Al₂O₃ catalyst in the steam gasification. The catalytic performance of the Co–Fe/ α -Al₂O₃ catalyst was much lower than that of Co–Fe/Mg/Al (10–10/40/40) (Fig. 10). Even on the fresh Co–Fe/ α -Al₂O₃, the deactivation of the catalyst was very severe at this low S/C (=0.23) reaction condition. The amount of the deposited carbon after the test of Fig. 12C was determined to be 3.8 mmol/g_{cat}, which was comparable to the case of Co–Fe/Mg/Al (10–10/40/40) and this suggests that coke deposition is not a main cause of the catalyst deactivation. In addition, the activity of Co–Fe/ α -Al₂O₃ decreased significantly with the repeated times, these results indicate that the regeneration ability of Co–Fe/ α -Al₂O₃ was much lower than that of Co–Fe/Mg/Al (10–10/40/40). Fig. 13 shows the XRD result of Co–Fe/ α -Al₂O₃ after the reduction and the catalytic use in Fig. 12. On the Co–Fe/ α -Al₂O₃ catalyst after the reduction pretreatment, Co rich Co–Fe fcc alloy and Fe rich Co–Fe bcc alloy were detected as reported previously [19]. After the catalytic use, the structure of the Co–Fe/ α -Al₂O₃ catalyst was changed, and the Co–Fe bcc alloy disappeared, in contrast, CoAl₂O₄ [64]

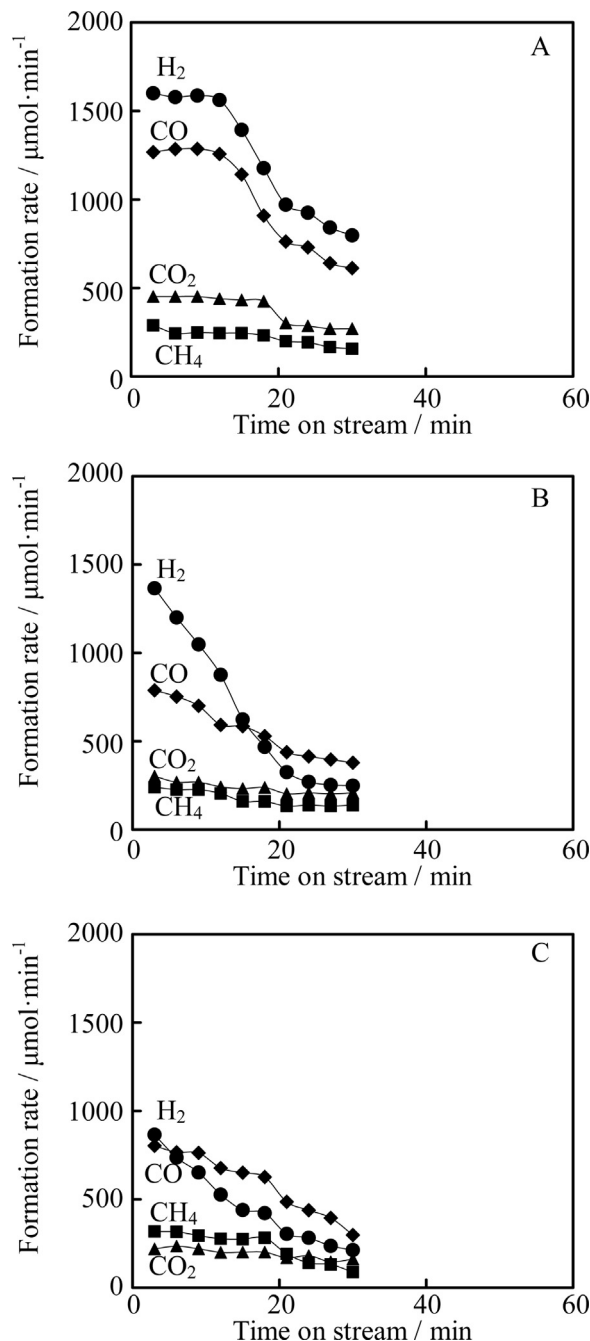


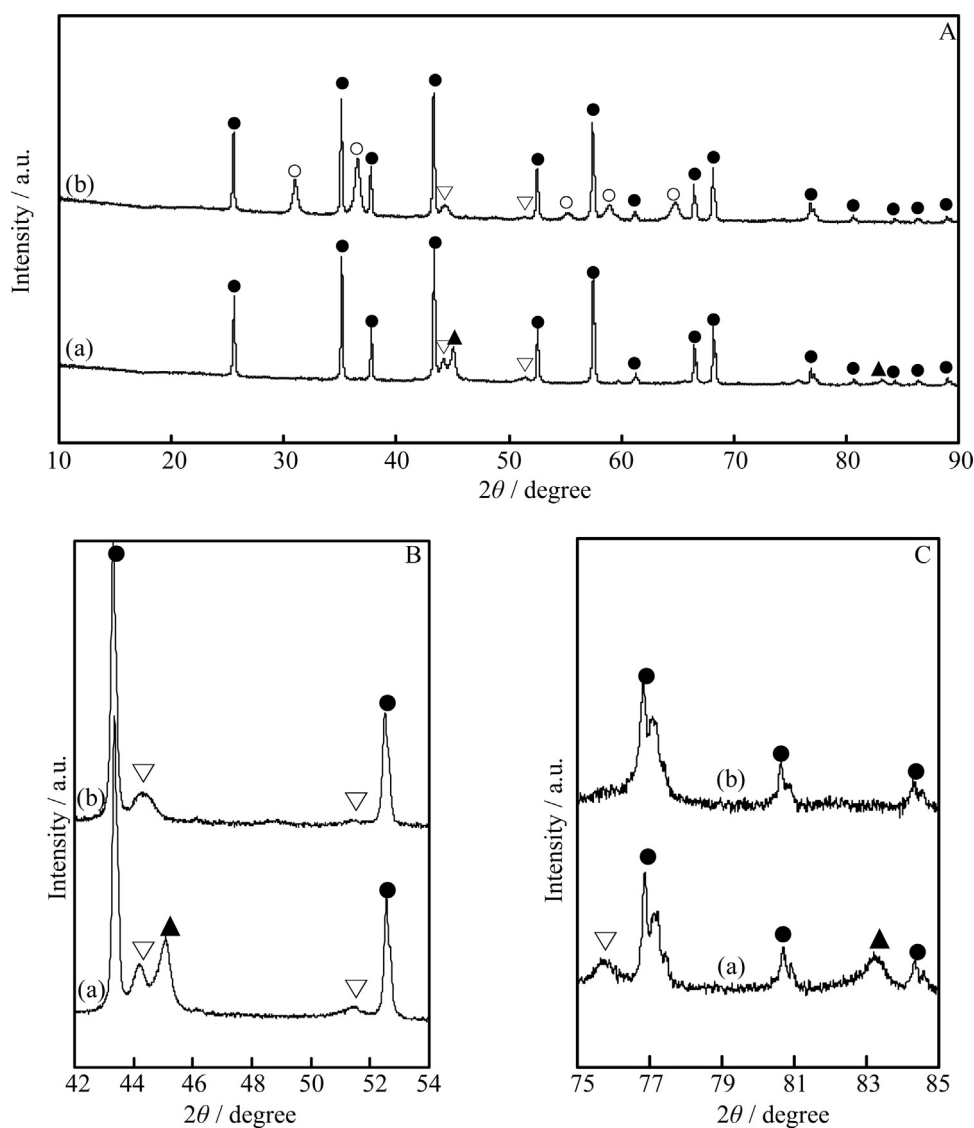
Fig. 12. Reaction time dependence of steam gasification of biomass-derived tar over Co–Fe/ α -Al₂O₃ at 873 K and S/C = 0.23. Catalyst weight was 0.3 g. (A) The fresh catalyst reduced at 773 K in H₂. (B) The used catalyst of (A) after the oxidation with O₂/N₂ (1/3) at 873 K for 1 h and the subsequent reduction at 773 K in H₂. (C) The used catalyst of (B) after the oxidation with O₂/N₂ (1/3) at 873 K for 1 h and the subsequent reduction at 773 K in H₂.

or FeAl₂O₄ phase [65] appeared. This behavior can be explained by the oxidation of Co and/or Fe species and subsequent solid phase reaction between these species and α -Al₂O₃ to form the mixed oxide during the catalytic use. The low regeneration ability of Co–Fe/ α -Al₂O₃ is interpreted by the structural change during the reaction and regeneration procedure. Higher regenerability of Co–Fe/Mg/Al (10–10/40/40) than Co–Fe/ α -Al₂O₃ can be related to the reactivity of the oxidized Co and Fe species with the oxide supports. In the case of Co–Fe/Mg/Al (10–10/40/40), MgO-based solid solution was formed during the catalytic use and regeneration procedure. This behavior has been also observed on Co/Mg/Al

Table 6

Curve fitting results of Co K- and Fe K-edge EXAFS of Co–Fe/Mg/Al (10–10/40/40) after the reaction.

Edge	Treatment	FF range ^a (10 ^{−1} nm)	Shells	CN ^b	R (10 ^{−1} nm) ^c	σ (10 ^{−1} nm) ^d	ΔE_0 (eV) ^e	R _f (%) ^f
Co K	Fig. 11A	1.258–2.762	Co–O	1.2	1.93	0.078	−9.8	0.5
			Co–Fe (or Co)	6.1	2.47	0.076	−3.8	
			Co–Fe (or Co)	4.6	2.79	0.077	−8.6	
	Fig. 11C	1.258–2.762	Co–O	1.6	1.93	0.078	−9.2	1.6
			Co–Fe (or Co)	5.8	2.47	0.077	−3.6	
			Co–Fe (or Co)	4.4	2.79	0.077	−7.5	
Fe K	Fig. 11A	1.044–2.670	Fe–O	1.2	1.86	0.062	−9.3	1.3
			Fe–O	1.8	2.04	0.060	9.0	
			Fe–Co (or Fe)	3.9	2.47	0.077	−2.8	
	Fig. 11C	1.044–2.670	Fe–Co (or Fe)	2.3	2.87	0.069	6.6	0.5
			Fe–O	1.6	1.86	0.062	−9.8	
			Fe–O	2.4	2.04	0.060	9.4	
			Fe–Co (or Fe)	2.6	2.48	0.073	−1.0	
			Fe–Co (or Fe)	1.6	2.87	0.074	5.3	

^a Fourier filtering range.^b Coordination number.^c Bond distance.^d Debye–Waller factor.^e Difference in the origin of photoelectron energy between the reference and the sample.^f Residual factor.**Fig. 13.** XRD patterns (A, B and C) of Co–Fe/ α -Al₂O₃ after the reduction pretreatment (a) and the catalytic use (b) Fig. 12C). ● = α -Al₂O₃, ○ = CoAl₂O₄ or FeAl₂O₄, ▽ = Co–Fe fcc alloy and ▲ = Co–Fe bcc alloy.

(10/40/50) [41]. As reported previously, the hydrotalcite-derived catalysts such as Ni/Mg/Al, Co/Mg/Al, Ni–Fe/Mg/Al have nanocomposite structure consisting of monometallic or bimetallic alloy particles and Mg- and Al- containing oxide particles. In the case of Co–Fe/Mg/Al (10–10/40/40), the nanocomposite structure consists of Co–Fe bimetallic particles (~14 nm) and MgAl_2O_4 (major)-+MgO (minor)-based solid solutions (~16 nm) calculated from the BET surface area ($108\text{ m}^2/\text{g}$). After the catalytic use, the distribution of MgO-based solid solution increased, and it is thought that the deactivation of metal species on MgO-based solid solution by the oxidation is more significant than that on MgAl_2O_4 -based solid solution.

4. Conclusions

- (1) Hydrotalcite-like precursors containing Co, Fe, Mg and Al gave nanocomposite materials consisting of Co–Fe alloy particles where Co atoms substitute Fe sites in bcc structure of Fe metal to give the solid solution and the oxide particles of MgAl_2O_4 -based solid solution by the calcination and the reduction pretreatment. In particular, the Co–Fe alloy nanoparticles have bcc structure at the composition of Co/Fe/Mg/Al = 10/10/40/40 as the atomic percentage, and the composition of each particle was more uniform than that on Co–Fe/ α - Al_2O_3 catalyst prepared by the impregnation method. The particle size of the Co–Fe bcc alloy particles was about 14 nm, and the size of MgAl_2O_4 -based solid solution was about 16 nm. The H_2 adsorption amount on the reduced catalyst of Co–Fe/Mg/Al (10–10/40/40) was much smaller than that expected from the particle size, suggesting that the H_2 adsorption is suppressed by the alloy formation.
- (2) Co–Fe/Mg/Al catalysts prepared from hydrotalcite-like precursor with various compositions were tested in the steam gasification of cedar wood, and the optimized composition of the catalysts were determined to be Co/Fe/Mg/Al = 10/10/40/40. The performance of the Co–Fe/Mg/Al (10–10/40/40) catalyst showed higher activity and higher resistance to coke deposition than Co–Fe/ α - Al_2O_3 (Fe/Co = 0.25), Co/Mg/Al (10/40/50) and Ni–Fe/Mg/Al (Ni/Fe/Mg/Al = 9.1/2.3/66/23) catalysts, which have been previously reported to be effective catalysts.
- (3) Co–Fe/Mg/Al (10–10/40/40) showed higher regenerability than Co–Fe/ α - Al_2O_3 (Fe/Co = 0.25) in the repeated use containing the coke removal with the combustion and the subsequent catalyst activation by the reduction treatment for the steam gasification. However, the decrease of the catalytic performance of Co–Fe/Mg/Al (10–10/40/40) was observed in the results of the repeated use. According to the characterization of the used catalyst, the structural change of MgAl_2O_4 -based solid solution to MgO-based solid solution was detected, and this suggests that Co–Fe bcc alloy particles on MgO-based solid solution are oxidized more easily than those on MgAl_2O_4 -based solid solution.

Acknowledgements

This work was supported by the Cabinet Office, Government of Japan through its “Funding Program for Next Generation World-Leading Researchers”.

Appendix A. Supplementary data

Supplementary data associated with this article can be found, in the online version, at <http://dx.doi.org/10.1016/j.apcatb.2014.06.021>.

References

- [1] G.W. Huber, S. Iborra, A. Corma, *Chem. Rev.* 106 (2006) 4044.
- [2] H. de Lasa, E. Salas, J. Mazumder, R. Lucky, *Chem. Rev.* 111 (2011) 5404.
- [3] D. Li, L. Wang, M. Koike, K. Tomishige, *J. Jpn. Petrol. Inst.* 56 (2013) 253.
- [4] D. Li, Y. Nakagawa, K. Tomishige, *Chin. J. Catal.* 33 (2012) 583.
- [5] J. Li, J. Liu, S. Liao, R. Yan, *Int. J. Hydrogen Energy* 35 (2010) 7399.
- [6] T. Wang, J. Chang, X. Cui, Q. Zhang, Y. Fu, *Fuel Process. Technol.* 87 (2006) 421.
- [7] A. Corujo, L. Yermán, B. Arizaga, M. Brusoni, J. Castiglioni, *Biomass Bioenergy* 34 (2010) 1695.
- [8] K. Tomishige, T. Kimura, J. Nishikawa, T. Miyazawa, K. Kunimori, *Catal. Commun.* 8 (2007) 1074.
- [9] T. Kimura, T. Miyazawa, J. Nishikawa, S. Kado, K. Okumura, T. Miyao, S. Naito, K. Kunimori, K. Tomishige, *Appl. Catal., B: Environ.* 68 (2006) 160.
- [10] J. Nishikawa, K. Nakamura, M. Asadullah, T. Miyazawa, K. Kunimori, K. Tomishige, *Catal. Today* 131 (2008) 146.
- [11] J. Nishikawa, T. Miyazawa, K. Nakamura, M. Asadullah, K. Kunimori, K. Tomishige, *Catal. Commun.* 9 (2008) 195.
- [12] K. Nakamura, T. Miyazawa, T. Sakurai, T. Miyao, S. Naito, N. Begum, K. Kunimori, K. Tomishige, *Appl. Catal., B: Environ.* 86 (2009) 36.
- [13] M. Koike, C. Ishikawa, D. Li, L. Wang, Y. Nakagawa, K. Tomishige, *Fuel* 103 (2013) 122.
- [14] L. Wang, D. Li, M. Koike, S. Koso, Y. Nakagawa, Y. Xu, K. Tomishige, *Appl. Catal., A: Gen.* 392 (2011) 248.
- [15] M. Koike, D. Li, Y. Nakagawa, K. Tomishige, *ChemSusChem* 5 (2012) 2312.
- [16] K. Tasaka, T. Furusawa, A. Tsutsumi, *Energy Fuels* 21 (2007) 590.
- [17] K. Tasaka, T. Furusawa, A. Tsutsumi, *Chem. Eng. Sci.* 62 (2007) 5558.
- [18] D. Li, C. Ishikawa, M. Koike, L. Wang, Y. Nakagawa, K. Tomishige, *Int. J. Hydrogen Energy* 38 (2013) 3572.
- [19] L. Wang, Y. Hisada, M. Koike, D. Li, H. Watanabe, Y. Nakagawa, K. Tomishige, *Appl. Catal., B: Environ.* 121–122 (2012) 95.
- [20] T. Furusawa, A. Tsutsumi, *Appl. Catal., A: Gen.* 278 (2005) 207.
- [21] T. Furusawa, A. Tsutsumi, *Appl. Catal., A: Gen.* 278 (2005) 195.
- [22] L. Wang, D. Li, M. Koike, H. Watanabe, Y. Xu, Y. Nakagawa, K. Tomishige, *Fuel* 112 (2013) 654.
- [23] M. Koike, Y. Hisada, L. Wang, D. Li, H. Watanabe, Y. Nakagawa, K. Tomishige, *Appl. Catal., B: Environ.* 140–141 (2013) 652.
- [24] K. Urasaki, K. Tokunaga, Y. Sekine, M. Matsukata, E. Kikuchi, *Catal. Commun.* 9 (2008) 600.
- [25] A. Kazama, Y. Sekine, K. Oyama, M. Matsukata, E. Kikuchi, *Appl. Catal., A: Gen.* 383 (2010) 96.
- [26] Y. Sekine, A. Kazama, Y. Izutsu, M. Matsukata, E. Kikuchi, *Catal. Lett.* 132 (2009) 329.
- [27] N. Iwasa, S. Masuda, N. Takezawa, *React. Kinet. Catal. Lett.* 55 (1995) 349.
- [28] X. Hu, G. Lu, *J. Mol. Catal. A: Chem.* 261 (2007) 43.
- [29] D.M. Alonso, S.G. Wettstein, J.A. Dumesic, *Chem. Soc. Rev.* 41 (2012) 8075.
- [30] M. Sankar, N. Dimitratos, P.J. Miedziak, P.P. Wells, C.J. Kiely, G.J. Hutchings, *Chem. Soc. Rev.* 41 (2012) 8099.
- [31] D. Li, Y. Nakagawa, K. Tomishige, *Appl. Catal., A: Gen.* 408 (2011) 1.
- [32] S. Hirasawa, H. Watanabe, T. Kizuka, Y. Nakagawa, K. Tomishige, *J. Catal.* 300 (2013) 205.
- [33] D. Świerczyński, S. Libs, C. Courson, A. Kiennemann, *Appl. Catal., B: Environ.* 74 (2007) 211.
- [34] J. Ashok, S. Kawi, *ACS Catal.* 4 (2013) 289.
- [35] U. Oemar, P.S. Ang, K. Hidayat, S. Kawi, *Int. J. Hydrogen Energy* 38 (2013) 5525.
- [36] U. Oemar, M.L. Ang, W.F. Hee, K. Hidayat, S. Kawi, *Appl. Catal., B: Environ.* 148–149 (2014) 231.
- [37] D. Li, M. Koike, L. Wang, Y. Nakagawa, Y. Xu, K. Tomishige, *ChemSusChem* 7 (2013) 510.
- [38] Y. Sekine, Y. Nakagawa, K. Oyama, T. Shimizu, S. Ogo, *Appl. Catal., A: Gen.* 472 (2014) 113.
- [39] T.B. Reed, *Free Energy Formation of Binary Compounds*, MIT, Press, Cambridge, MA, 1971, pp. 66.
- [40] S. Miyata, *Clays Clay Miner.* 23 (1975) 369.
- [41] L. Wang, D. Li, H. Watanabe, M. Tamura, Y. Nakagawa, K. Tomishige, *Appl. Catal., B: Environ.* 150–151 (2014) 82.
- [42] R.C. Reuel, C.H. Bartholomew, *J. Catal.* 85 (1984) 63.
- [43] Y. Chen, K. Tomishige, K. Yokoyama, K. Fujimoto, *Appl. Catal., A: Gen.* 165 (1997) 335.
- [44] K. Tomishige, K. Asakura, Y. Iwasawa, *J. Catal.* 149 (1994) 70.
- [45] S. Koso, H. Watanabe, K. Okumura, Y. Nakagawa, K. Tomishige, *Appl. Catal., B: Environ.* 111–112 (2012) 27.
- [46] F. Cavani, F. Trifirò, A. Vaccari, *Catal. Today* 11 (1991) 173.
- [47] R. Shannon, *Acta Crystallogr., Sect. A: Found. Crystallogr.* 32 (1976) 751.
- [48] X-Ray Powder Diffraction Data File, ICSD 96837.
- [49] X-Ray Powder Diffraction Data File, ICSD 9863.
- [50] D. Li, L. Wang, M. Koike, Y. Nakagawa, K. Tomishige, *Appl. Catal., B: Environ.* 102 (2011) 528.
- [51] L.H. Bennett, B.C. Giessen, T.B. Massalski, *Book Alloy Phase Diagrams*, 1984.
- [52] G.A. Prinz, *Phys. Rev. Lett.* 54 (1985) 1051.
- [53] X-Ray Powder Diffraction Data File, ICSD 155839.
- [54] J.T.E. Whyte, *Catal. Rev.* 8 (1973) 117.
- [55] F. Tielens, M. Calatayud, R. Franco, J.M. Recio, J. Pérez-Ramírez, C. Minot, *J. Phys. Chem. B* 110 (2006) 988.
- [56] H.J. Jung, M.A. Vannice, L.N. Mulay, R.M. Stanfield, W.N. Delgass, *J. Catal.* 76 (1982) 208.

- [57] J. Sehested, *Catal. Today* 111 (2006) 103.
- [58] K. Tomishige, Y. Himeno, Y. Matsuo, Y. Yoshinaga, K. Fujimoto, *Ind. Eng. Chem. Res.* 39 (2000) 1891.
- [59] Y. Chen, K. Tomishige, K. Fujimoto, *Appl. Catal., A: Gen.* 161 (1997) L11.
- [60] M. Nurunnabi, Y. Mukainakano, S. Kado, B. Li, K. Kunimori, K. Suzuki, K. Fujimoto, K. Tomishige, *Appl. Catal., A: Gen.* 299 (2006) 145.
- [61] K. Tomishige, *Catal. Today* 89 (2004) 405.
- [62] M. Asadullah, S. Ito, K. Kunimori, K. Tomishige, *Ind. Eng. Chem. Res.* 41 (2002) 4567.
- [63] T. Miyazawa, K. Okumura, K. Kunimori, K. Tomishige, *J. Phys. Chem. C* 112 (2008) 2574.
- [64] X-Ray Powder Diffraction Data File, ICSD 40029.
- [65] X-Ray Powder Diffraction Data File, ICSD 74612.